Yoshikawa et al. ROBOMECH Journal (2023) 10:18
https://doi.org/10.1186/s40648-023-00257-9

ROBOMECH Journal

RESEARCH ARTICLE Open Access

# A single motor-driven continuum robot that can be designed to deform into a complex shape with curvature distribution

Daiki Yoshikawa[1*], Masahiro Shimizu[2] and Takuya Umedachi[1]

**Abstract**

This paper proposes a method to deform a continuum robot into a complex shape with distributed curvature using a single motor drive. This continuum robot can be deformed to a desired shape by placing tendon guides at appropriate intervals. We used several target shapes, including clothoid and sin curves, as well as a circular curve of constant curvature and confirmed that the deformed shapes match them both in the simulation and prototype. This paper proposes two models of continuum robots. One is the Plain Model in which the tendons are parallel to the rod and the Penetration Model in which the tendon penetrates to the rod. By placing the penetrating position(s), this continuum robot can be deformed into a shape with inflection point(s). We designed a mathematical model to simulate the deformed shape of the prototype to obtain the proper placement of the guides and penetration point(s). Through the optimization, it was able to find the parameters that, in most cases, result in the error of less than 4% between the target and deformed shapes on simulation. We applied these conditions to the prototype and evaluated the errors, which were approximately 10%, the same as the related works that use a conventional constant curvature model. We think that the results of this paper can be applied to reduce the number of actuators required and the size and weight of continuum or biomimetic robots.

**Keywords** Continuum robot, Optimization, Tendon driven

## Introduction

The advantages of continuum robots include mechanical flexibility and interactivity with their surroundings. Snake-like robots [1, 2] are similar in the shape and have a long history; however, the features of continuum robots can extend the application fields. In the medical field, these robots are used mainly in minimally invasive surgery [3, 4]. Medical robots are responsible for examining and treating the affected areas while flexibly deforming their bodies to avoid damaging the patient's body tissues. As a disaster response robot, it is practical to locate objects in collapsed debris [5, 6]. This mechanism is also used as a manipulator with high grasping capability. They are expected to operate in particular environments, such as underwater and space [7–9]. Such continuum robots are widely modeled as constant curvature models. These robots have infinite degrees of freedom [10, 11] and continuum part(s), whose curve can be approximated with continuous tangent vectors [12, 13].

Tendon drive is one of the typical drive mechanisms for continuum robots. Many such continuum robots employ flexible rods threaded with tendons through multiple guides (e.g., [14–16]). The guides are placed at regular intervals. The deformation of the rods between the guides is assumed to be a circular curve of constant curvature [17].

Designing the deformation shape of the entire mechanism, rather than focusing only on the end-effector's

*Correspondence:
Daiki Yoshikawa
22fs323a@shinshu-u.ac.jp
[1] Shinshu University, Ueda, Japan
[2] Nagahama Institute of Bio-Science and Technology, Nagahama, Japan

© The Author(s) 2023. **Open Access** This article is licensed under a Creative Commons Attribution 4.0 International License, which permits use, sharing, adaptation, distribution and reproduction in any medium or format, as long as you give appropriate credit to the original author(s) and the source, provide a link to the Creative Commons licence, and indicate if changes were made. The images or other third party material in this article are included in the article's Creative Commons licence, unless indicated otherwise in a credit line to the material. If material is not included in the article's Creative Commons licence and your intended use is not permitted by statutory regulation or exceeds the permitted use, you will need to obtain permission directly from the copyright holder. To view a copy of this licence, visit http://creativecommons.org/licenses/by/4.0/.

position, will enhance the application value of continuum robots. The shape that is interacting with the environment does not have constant curvature in many cases. Therefore, the continuum robot can further flexibly adapt and perform tasks such as searching and grasping by deforming itself to suit its surrounding environment and a grasped object. However, with the traditional constant curvature model, it is necessary to use multiple actuators to have the deformed shape's curvature distribution. This will increase the weight and size of the entire prototype.

There are previous works that use a single actuator to obtain multiple curvatures. For example, Oliver-Butler et al. [18] obtained changeable curvature by varying the distance between the routed tendon and rod. In this study, the distance is given by a linear equation. Pogue et al. [19] achieved this by a magnetically-actuated locking mechanism, which requires the application of an external magnetic field. This study requires additional parts (magnets, motors) for more complex deformations.

This paper proposes a continuum robot that can deform along non-constant-curvature shapes (e.g., clothoid curve, lemniscate, and omega shape) driven by a single motor. This can be realized by designing segment lengths separated by guides. The proposed tendon-driven continuum robot configuration is a model in which the tendon is threaded through the guides to be parallel to the rod (Plain Model). To simulate the complex deformation, we developed a mathematical model. This model is used to optimize segment lengths and the winding tendon so that the deformed shape matches the target shape. Based on the parameters obtained from the optimization, we drove the prototype and confirmed that the shapes matched with the desired shapes. This method can also be applied with the tendon penetrating the rod (Penetration Model). Since the methods can complicatedly deform with a single drive, designing smaller and lighter continuum robots for complex deformations is possible.

## Proposed method

This section describes the components of the prototype and the proposed method for producing complex deformations. In the first subsection, we illustrate the robot components. The second subsection explains the models that we tested. The third subsection consists of three parts: the first explicates the mathematical modeling of the robot components, the second explicates how to simulate the deformed shape, and the third describes the optimization procedure to make the deformed shape match the target shape. The variables and constants are defined in Table 1.

### Continuum robot design

The continuum robot in this study is mainly composed of circular discs as the tendon guides (Fig. 1a), a flexible rod (Fig. 1b), two tendons, and a tendon pulling mechanism with a single motor (POLOLU-3078) that winds the tendons (Fig. 1c). The flexible rod is made of TPU (Thermoplastic Polyurethane resin, TPU95A, Ultimaker) and fabricated by a 3D printer (Raise3D E2, Raise3D Technologies Inc). The solid discs were made using chopped fiber CFRP (nylon/CCF material, Onyx, Markforged) as the material and were fabricated them using a 3D printer (Mark Two, Markforged). The rod has a circular cross section with a diameter of 4 mm and has a 1.3 mm × 0.4 mm groove in the axial direction across the entire rod (Fig. 1b, left). The discs are secured in position along the rod by fitting their protrusions into other circumference grooves placed at regular intervals in the rod (Fig. 1b, right). The discs are 3 mm thick (Fig. 1a). The holes in the center of the discs are used for passing the rod. In addition, several holes (here in after called 'guide holes') are drilled in the discs to thread the tendons through.

The distance between the discs can be adjusted freely, and the rod is deformed by pulling a tendon through the discs. The rod and discs are assembled such that the protrusion part of the discs can fit into the rod grooves, so that the discs do not rotate around the rod. The tendon is threaded through the guide holes. The disc placed at the endpoint of the rod is secured to one endpoint of the tendon by Fixture 1 (Fig. 1d). The other endpoint of the tendon is secured to the pulley (Fig. 1f). Fixture 2 (Fig. 1e) constrains the positional relationship between the rod and the motor. The rod is deformed by winding

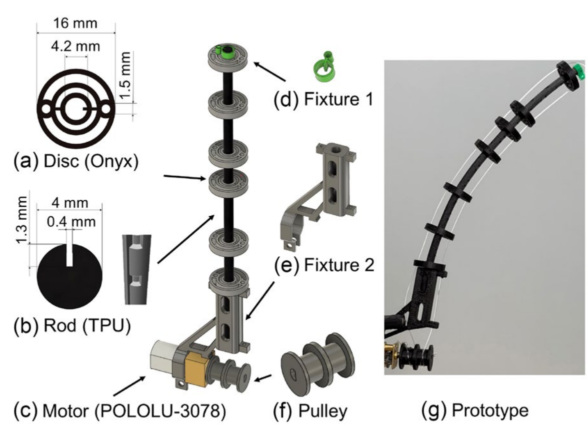


**Fig. 1** The parts that make up the prototype and appearance of the prototype. **a**, **b** The disc and rod's cross-sectional shape and the rod's side. **c** Driving motor. **d** Fixture 1 for attaching to the end of the rod and securing the tendon. **e** Fixture 2 that holds the motor and rod in place. **f** Pulley for winding the tendon. **g** Driving the prototype

the tendon using the motor (Fig. 1g). The design assumes that the tendons do not sag when the rod deforms.

Another tendon is placed antagonistically in the same way, and a single motor drives these two tendons to deform the rod in opposite directions. When restoring the shape of the rod, it is necessary to wind one tendon and feed another tendon simultaneously. Therefore, as shown in Fig. 1f, a pulley with a partition was designed to prevent the tendons from tangling with each other.

## Proposed wiring methods

### *Plain model*

As shown in Fig. 2a, the Plain Model is a simple model with two tendons stretched parallel to the axial direction of the rod.

### *Penetration model*

To realize S-shape deformation, we propose the Penetration Model in which the tendons penetrate the rod as shown in Fig. 2b. In this model, we make one or more holes in the rod so the tendons can be passed through. This can be mathematically modeled by modifying the Plain Model.

## Procedures for the rod's shape simulation and optimization

We propose a mathematical simulation that considers tendon tension differences between the rod segments, making it possible to search for conditions under which the deformed shape matches the target shape. The target shape can be not only a circular curve with constant curvature but also a complex deformation. Grasshopper, a modeling support tool of Rhino 6, a 3DCAD software with a parametric design feature, is used for realizing the simulation. In addition, the physics simulator plug-in Kangaroo2 and optimization plug-in Octopus are also used.

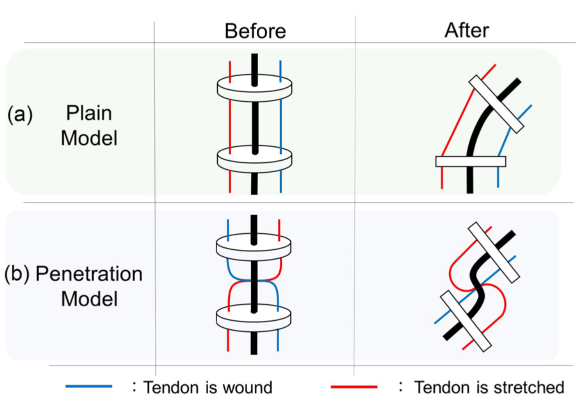


**Fig. 2** How to thread the tendons and the shape after deformation of each model. **a** Plain Model. **b** Penetration Model

### *Mathematical model of the rod segment and tendon*

We modeled the rod segment with linear and torsion springs. In this study, the rod is modeled with three linear springs and two torsion springs per 10 mm. The tendon section is modeled as linear springs, as illustrated in Fig. 3a. The discs of the prototype are modeled as a spring, a damper, and "two" torsion springs, as shown in Fig. 3b. The disc model can be attached to the rod at the connection points (Fig. 3(a)) of any rod's linear springs, and the tendon is attached to the connection points of the disc model's.

The discs are not deformable. We define the disc-model's linear springs are sufficiently stiff and their length is $R$. Precisely, the disc part (in Fig. 3) should be defined as a rigid body to constrain the relative positions of the rod and disc (i.e., tendon). However, the discs are defined as stiff springs (Fig. 3b) to simplify the simulation model. The torsion spring on the rod side constrain to be at a right angle between the rod and the discs. Meanwhile, weak torsion springs are installed to simulate the bending stiffness of the tendon around the disc-models.

We determined the tendon's linear spring constant ($k_{\mathrm{L,t}}$) and the rod's torsion spring constant ($k_{\mathrm{T,r}}$) to simulate the prototype's deformation as follows. The linear springs were assumed to be sufficiently stiff ($k_{\mathrm{L,t}} = 2 \cdot 10^4$ N/m). $k_{\mathrm{T,r}}$ was approximately defined from the classical cantilever beam deflection equation [18] and the relation between the torsion spring constant and torque:

$$k_{\mathrm{T,r}} = \frac{3EI}{L}, \tag{1}$$

where $I$ is the sectional secondary moment of the rod, $E$ is Young's modulus of TPU and $L$ is the total length of the rod (Fig. 4a). We determined the appropriate value to simulate the bending of the prototype's rod.

The entire continuum mechanism is modeled as a series of segments (Fig. 3d) separated by the discs. The entire continuum mechanism is modeled as $N$ segments, which are divided by $N + 1$ discs. The natural length of the tendon at the $n$th ($1 \leq n \leq N$) segment is $L_n$, and the actual length of the tendon after deformation is $l_n$. This value corresponds to the tendon length between the discs on deforming the prototype (Fig. 4b). When simulating the Plain Model (Fig. 3(a)), we define $L_n(t = 0) = (1 - w/L)d_n$, where $d_n$ is the natural length of the rod in the $n$th segment. This value can also be the length between the disc and disc (Fig. 4a). $w$ is the length of the tendon winding. When simulating the Penetration Model (Fig. 3c), we define $j$ as the segment number to be drilled. The $L_j(0)$ is calculated as:

$$L_j(t = 0) = (1 - w/L)\sqrt{d_j^2 + (2R)^2}, \tag{2}$$

and the tendon's center point is anchored at the connection point of the center of the $j$th segment. The sum of

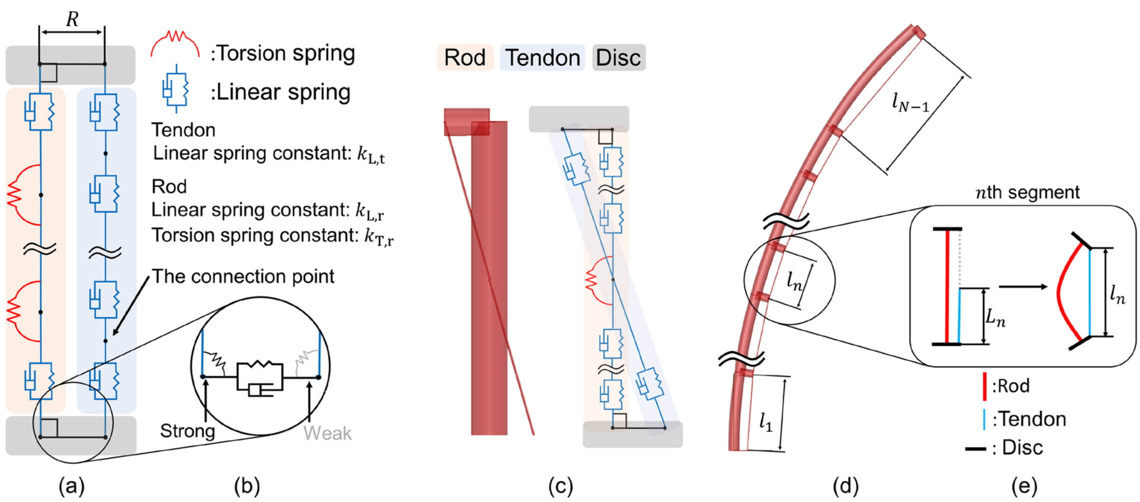


**Fig. 3** Mathematical model of the rod deformation and deformed-shape optimization. **a** We define the rod as linear and torsion springs for each interval separated by the disc. **b** The connection points of the tendon and segment are restrained with torsion springs of different strengths. **c** Mathematical model of the Penetration Model. The connection points of the tendon are constrained at the center of the segment. **d** The segments are parts of the rod between the discs. **e** The rod deforms like a bow for each segment, and the tendon's linear springs are stretched to generate different tensions

$L_n$ plus $w$ equals the total length of the rod. $L_n$ is shorter than the natural length of the rod in the $n$th segment.

### *Simulation of the deformed rod shape*

When the motor pulls the tendon, the tendon is tense due to the difference between the actual and natural lengths

**Table 1** List of valuables and parameters used in the mathematical models

| | |
|---|---|
| $d_n$ [mm] | Rod segment's length between the $n$th disc and the $n+1$th disc. |
| $L_n$ [mm] | Natural length of the tendon between $n$th disc and $n+1$th disc. |
| $l_n$ [mm] | Actual length of the tendon between $n$th disc and $n+1$th disc. |
| $T_n$ [N] | Tension generated in the tendon between $n$th disc and $n+1$th disc. |
| $w$ [mm] | Length of the tendon to be wound. |
| $L$ [mm] | Total length of the rod. |
| $R$ [mm] | Radius of the disc. |
| $E$ [N/mm$^2$] | Young's modulus of the rod. |
| $I$ [mm$^4$] | The rod's cross-sectional secondary moment. |
| $N+1$ | Number of discs. |
| $M$ | Number of representative points and target points. |
| $k_{T,r}$ [N·m/rad] | Torsion spring constant of the rod. |
| $k_{L,r}$ [N/mm] | Linear spring constant of the rod. |
| $k_{L,t}$ [N/mm] | Linear spring constant of the tendon. |

of the tendon. This causes each segment to deform in a bow-like shape (Fig. 3e). Hooke's law can be used to calculate the tension in the tendon between the guides (discs in the prototype).

In the case of an actual tendon, the tendon moves across the discs. Also, for all segments, the tension in the tendon eventually reaches the same value, i.e., there is an equilibrium between segments. However, in the simulation model, there will be a difference in tension between adjacent segments. To remove the gap between the actual tendon and simulation, we propose to redistribute the natural length of the tendon between adjacent segments according to the difference in tension. The redistribution algorithm should change the natural length of segment tendons at the next time step so as to decrease the tension difference between neighboring segment tendons. Specifically, in the recursive algorithm, $L_n(t)$ is the $L_n$ at $t$,

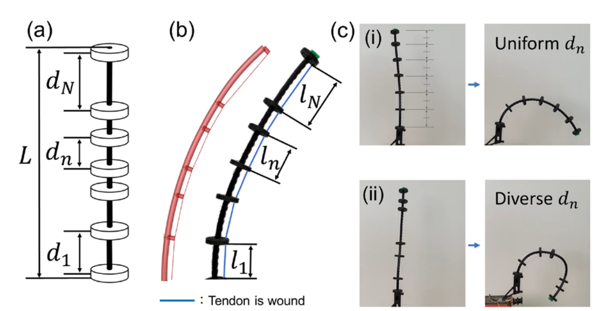


**Fig. 4** **a** The prototype design variables. **b** Correspondence between the simulation and the prototype. **c** Difference in deformed shape of the prototypes. (i) In case the disc is placed at regular intervals. (ii) In case the disc is not placed at regular intervals

$L_n$ of the next step is $L_n(t + \Delta t)$, and the tendon tension is $T_n(t)$ can be written as follows:

$$L_n(t + \Delta t) - L_n(t) = -\tau(T_n(t) - (T_{n-1}(t) + T_{n+1}(t))/2) \tag{3}$$

$$T_n(t) = -k_{\mathrm{L,t}}(L_n(t) - l_n(t)) \tag{4}$$

where $T_0(t) = T_2(t)$, $T_{N+1}(t) = T_{N-1}(t)$, and $\tau$ is a time constant. The recursive algorithm terminates when the tension difference is sufficiently slight for each segment (concretely, when tension difference $\leq 1.0 \cdot 10^{-4}$ N).

### *Optimization of the rod's deformation shape*

The prototype can deform into a complex shape with diverse $d_n$ (Fig. 4c). We optimize the position of the disc to make the deformed shape closer to the target shape. Figure 5 shows the flow chart of the optimization. We simulate the rod's deformation by considering the tension difference in the tendon between each segment.

$M$ representative points (Fig. 6, red points) are arranged to equally divide the total length of the rod into $M + 1$ parts. Target points (Fig. 6, yellow points) are arranged at equal intervals on the target shape. The distance between adjacent representative points must equal the distance between the target points along the curve. Let $(x_m, y_m)$ be the coordinates of the $m$th $(1 \leq m \leq M)$ representative point and $(x_{\mathrm{t},m}, y_{\mathrm{t},m})$ be the coordinates of the corresponding target point. In this study, optimization by a genetic algorithm is performed to minimize the following objective function:

$$z = \sum_{m=1}^{M} \{(x_m - x_{\mathrm{t},m})^2 + (y_m - x_{\mathrm{t},m})^2\}, \tag{5}$$

where the input is the coordinates of the target point $(x_{\mathrm{t},m}, y_{\mathrm{t},m})$. The genes are $d_n$ and $w$. We calculate the fitness from Eq. (5).

We evaluated the errors of the simulation's deformed shapes for the total rod length, $L$. We used the root mean square (RMS) of the distance between the target and the representative point pair. The shape's error evaluation formula, $E(z)$, can be expressed as shown in Eq. (6).

$$E(z) = \sqrt{\frac{z}{ML^2}}. \tag{6}$$

The optimization algorithm terminates when the value of Eq. (5) is below a threshold value ($z \leq 1$) and the generation number is above a threshold value (generation number $\geq 100$). This method can simulate a deformed shape of a tendon-driven continuum robot when the tendon tension can be calculated.

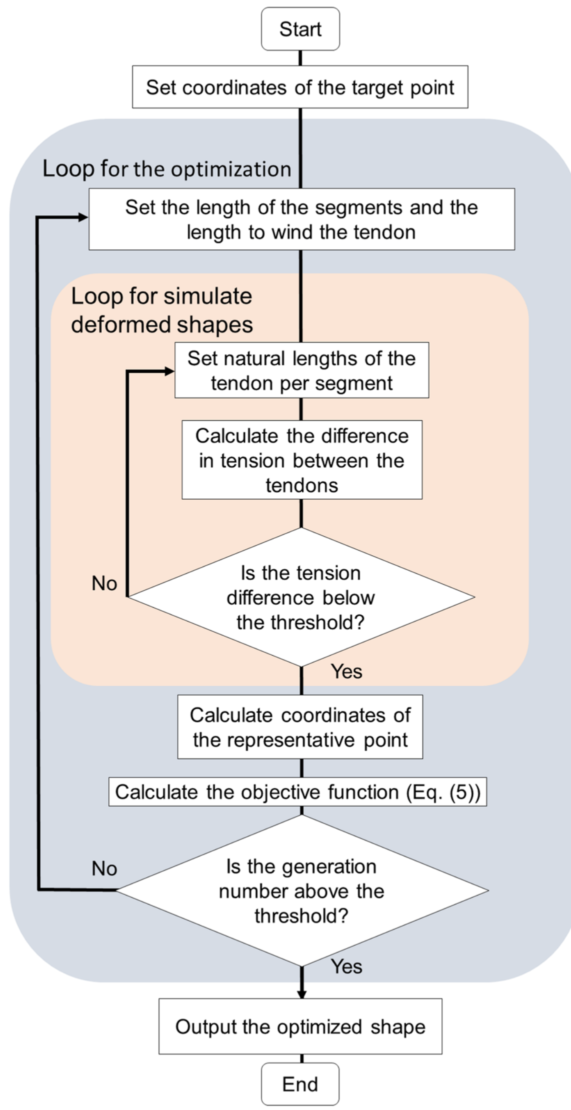


**Fig. 5** Flowchart of the shape optimization

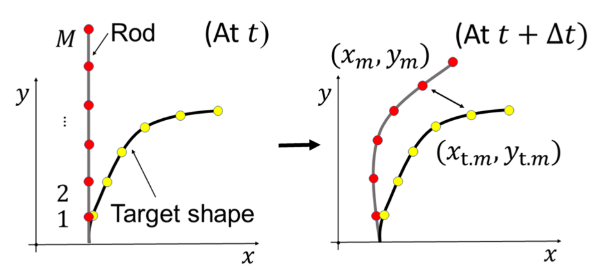


**Fig. 6** The representative points and target points. The distance between the point pairs gets closer with time evolution

## Result

For the Plain Model and the two different Penetration Models, we optimized the winding length of the tendon, $w$, the segment lengths, $d_n$, and the segment number to be drilled, $j$, so that the deformed shapes of the rod approach the target shapes. We selected three target shapes for each model.

We used Eq. (6) to evaluate the error between the deformed shape and the target shapes. We used a fixed camera and image processing software (Click Measure [20]) to measure the distances between the target points and representative points on the prototype. Note that the error does not contain the in- and out of direction of the design plane ($xy$-plane in Fig. 6)

### Plain model

We used the curves shown in the upper row in Fig. 7 as the target shapes. The first is a circular curve (the top plot in Fig. 7a). This is often used to approximate the shape of a continuum mechanism in the constant curvature model in related works. The second is a clothoid curve (the top plot in Fig. 7b) with a curvature that increases proportionately to the curve length from the starting point. This curve is expressed as $\kappa = As$, where $\kappa$ is the curvature, $s$ is the curve length, and $A$ is an arbitrary constant. The third is a lemniscate curve (the top plot in Fig. 7c) with a curvature that is a nonlinear function. This curve is expressed using a polar equation as $r^2 = a^2 \cos 2(\theta - \pi/4)$, where $a$ is an arbitrary constant.

#### *Optimization setup of plain model*

The total length of the deformed rod part is 180 mm. The target shapes are similarly enlarged so that the curve length is the same as the rod. We define $N = M = 6$ (i.e., set six representative points on the simulated rod and target points on the target shape). We also set the minimum segment length to 5 mm, the maximum to 90 mm, and the increment to 5 mm. For the winding tendon length, we set the minimum to 1 mm, the maximum to 125 mm, and the increment to 1 mm.

#### *Simulation results of plain model*

Table 2 shows the parameter values (the wound length of the tendon, $w$, and the initial length value between each segment, $d_n$) obtained by the optimization. The middle row in Fig. 7 shows the simulation results. Figure 8 (blue, Target-Simulation) shows the errors between the target shapes and the simulated deformed shapes. The values were calculated using Eq. (6). The results show that the errors between the target shapes and the simulations are

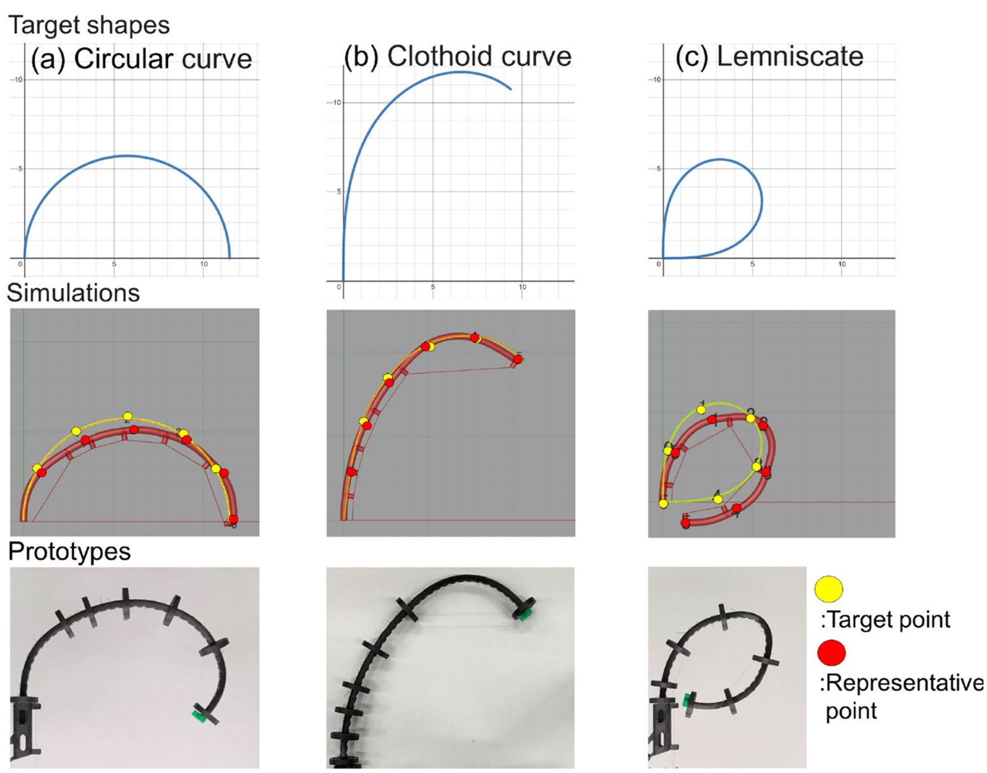


**Fig. 7** Target shapes and deformed shapes of simulations and prototypes. Deformed shapes are achieved by optimization of Plain Model. **a** Circular curve. **b** Clothoid curve. **c** Lemniscate

less than 6%. Especially when the clothoid curve is the target shape, the error is less than 2%.

### *Prototype results of plain model*

We drove the prototype based on the parameters obtained from the optimization and observed the deformation. The bottom row in Fig. 7 shows the prototype's shapes after deformation. We evaluated the prototype in the same way as the simulation. Figure 8 shows the experimental results, i.e., the errors between target shapes and prototype deformations (orange, Target-Prototype). The errors are generally the same for the three curves, remaining less than 9%.

## Penetration model (i)

Next, we used curves whose curvatures are reversed once, such at the S-shaped curve and sinusoidal curve at the target shapes. The curves shown in the upper row of Fig. 9 are the target shapes. The first is a curve consisting of two half circles (the top plot in Fig. 9(a)). The second is a sin curve (the top plot in Fig. 9(b)), which uses the shape of a curve with one period. The third is a curve that is an extension of a sin curve (the top plot in Fig. 9(c)) [21]. This expression, $h_f(x)$, can be written as follows:

$$h_f(x) = (c_1 x + c_2 x^2)\sin(kx). \tag{7}$$

We drill the hole in the center of the segment where the tendon penetrates the rod.

### *Optimization setup of penetration model (i)*

The optimization determines the $j$th segment to be drilled, $w$, and $d_n$. We define $N = 6$ guides and $M = 9$ representative points. We also set the minimum segment length to 5 mm, the maximum segment length to 50 mm, and the increment to 5 mm. For the winding tendon length, we set the minimum to 1 mm, the maximum to 75 mm, and the increment to 1 mm. Other conditions are the same as in the optimization of the Plain Model.

### *Simulation results of penetration model (i)*

Table 3 shows the parameter values ($j$, $w$, and $d_n$) obtained by the optimization. The tendon penetrates the rod at an inflection point on the target shapes.

### *Prototype results of penetration model (i)*

The bottom row in Fig. 9 shows the prototype's shapes after deformation. Figure 10 shows the experimental results, i.e., the errors between the target shapes and prototype deformations (orange, Target-Prototype). The errors are larger than that in the simulation results, yet they remain less than 12%.

**Table 2** Optimization result of the Plain Model

| Unit [mm] | $w$ | $d_1$ | $d_2$ | $d_3$ | $d_4$ | $d_5$ | $d_6$ |
|---|---|---|---|---|---|---|---|
| (a) Circular curve | 37 | 50 | 15 | 20 | 25 | 30 | 40 |
| (b) Clothoid curve | 26 | 15 | 15 | 15 | 25 | 30 | 80 |
| (c) Lemniscate | 59 | 10 | 25 | 35 | 50 | 35 | 25 |

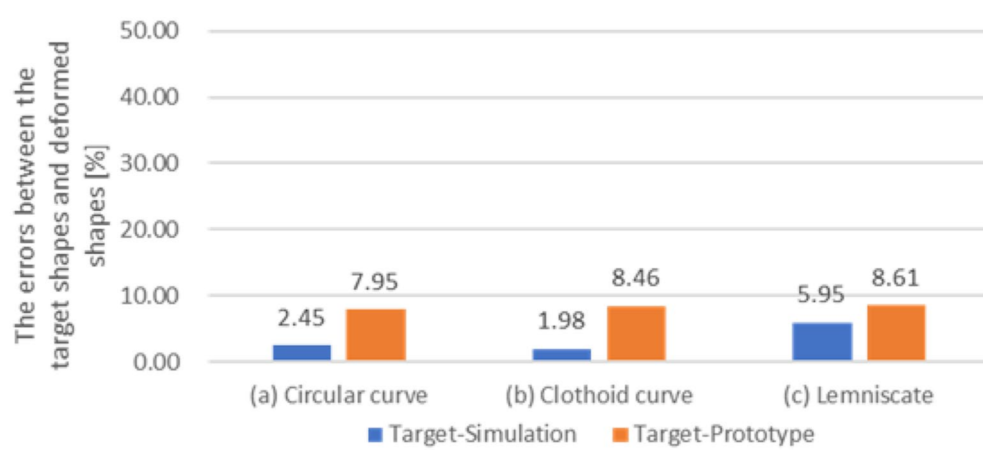


**Fig. 8** The error comparison between the target and deformed shapes (simulation and prototype). The value is calculated from Eq. (6)

**Penetration model (ii)**

We verified the effectiveness of the proposed method for the target shapes where the curvature is reversed twice. In other words, we observed the deformed shape when the rod had two holes where the tendon penetrates. We used the target shapes obtained from the approximation given in a previous work[22] (Fig. 11, upper row). There are two reasons for adopting these curves. First, we can

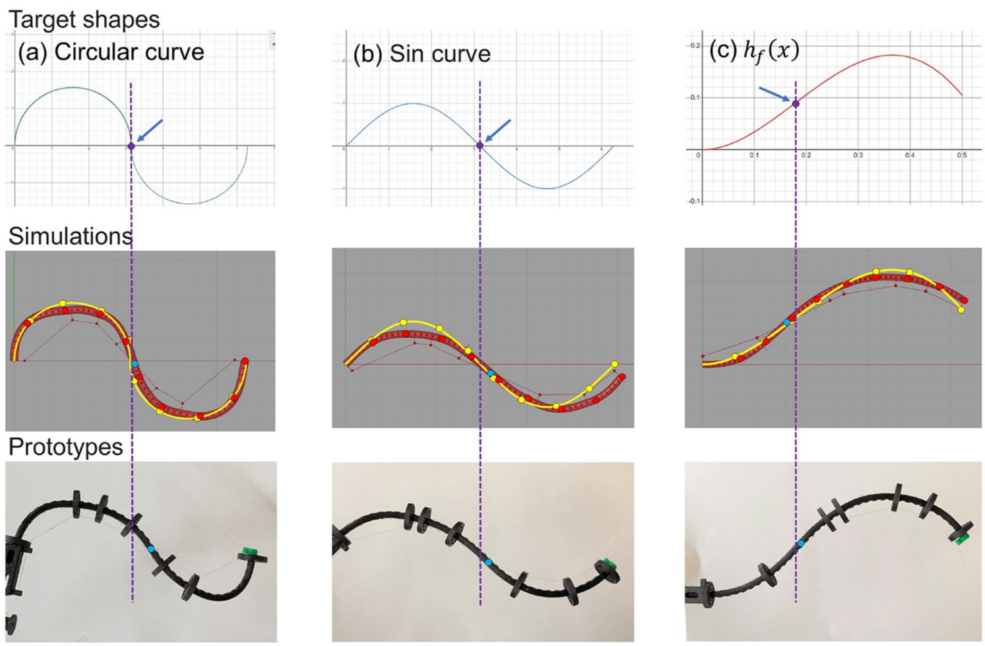


**Fig. 9** Target shapes and deformed shapes of simulations and prototypes. Deformed shapes are achieved by optimization of Penetration Model (i). The point indicated by the arrow is the inflection point of the simulations and prototypes. The blue points are the inflection points of the target shapes. **a** Circular curve. **b** Sin curve. **c** $h_f(x)$

**Table 3** Optimization result of Penetration Model (i)

| Unit [mm] | $j$ | $w$ | $d_1$ | $d_2$ | $d_3$ | $d_4$ | $d_5$ | $d_6$ |
|---|---|---|---|---|---|---|---|---|
| (a) Circular curve | 4 | 49 | 45 | 15 | 20 | 30 | 20 | 50 |
| (b) Sin curve | 4 | 25 | 45 | 10 | 20 | 50 | 30 | 25 |
| (c) $h_f(x)$ | 2 | 16 | 40 | 50 | 10 | 35 | 20 | 25 |

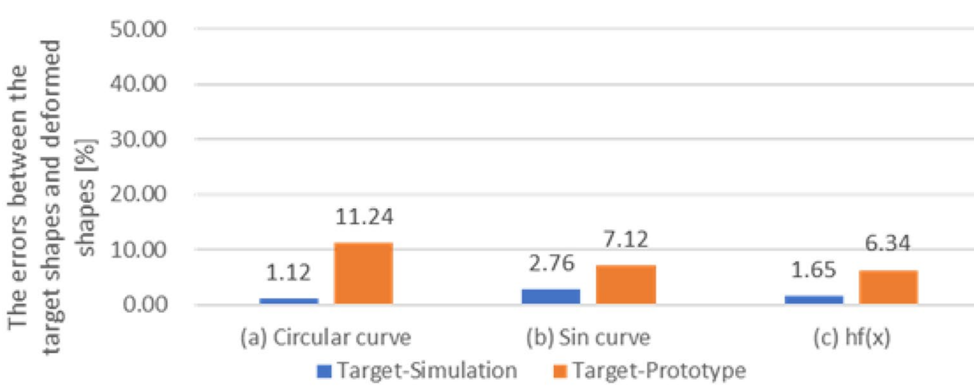


**Fig. 10** The error comparison between the target and deformed shapes (Penetration Model (i))

obtain different curves by changing a single parameter. The second is that this curve always has two reversal points of curvature. The approximation used is proposed as a mathematical model of a flexible beam with linear elasticity and is given by

$$x = \int_0^t \cos(B\sin(2\pi s))ds$$
$$y = \int_0^t \sin(B\sin(2\pi s))ds, \quad (0 \le t \le 1) \tag{8}$$

$$B = 2.22 - 0.281b - 4.533b^2 + 6.385b^3 - 3.494b^4, \quad (0.3 \le b \le 0.912) \tag{9}$$

where $b$ is an arbitrary constant. By changing the value of $b$, we can obtain all target shapes used in this study while keeping the same curve length.

### *Optimization setup of penetration model (ii)*

We optimized the parameters ($w$ and $d_n$) so that the deformed shapes match the target shapes at $b = 0.912$, 0.606, 0.3 in Eqs. (8) and (9). In this experiment, we drilled holes in the second and fourth segments ($j = 2$, 4). The total length of the deformed rod part was 150 mm. We defined $N + 1 = M = 6$. Other conditions of $w$ and $d_n$ were the same as in Penetration Model (i) optimization.

### *Simulation results of penetration model (ii)*

Table 4 shows the parameter values ($w$ and $d_n$) obtained by the optimization. The middle row in Fig. 11 shows the simulation results. Figure 11 (blue, Target-Simulation) shows the errors between the target shapes and the simulation's deformed shapes. Although the errors are larger than that in Penetration Model (i), they are still less than 4%.

### *Prototype results of penetration model (ii)*

The bottom row in Fig. 11 shows the prototype's shapes after deformation. Figure 12 shows the experimental results, the errors between the target shapes and prototype deformation (orange, Target-Prototype). For the deformed shape with $b = 0.3$, the maximum value of $w$ is selected.

## Discussion

The errors in the simulations were generally less than 4%. The distance, $d_n$, between the discs tended to be longer when the curvature of the target shape was more significant. The shape's error increased for shapes with larger deformation (e.g., Fig. 7 (c)).

All the prototype error values exceeded the simulation's error rates. We confirmed larger errors between the target points and the representative points along the rod toward the rod's tip. The friction between the tendon, disc, and rod was not considered in the simulation, which may have caused the increased error value in the prototype.

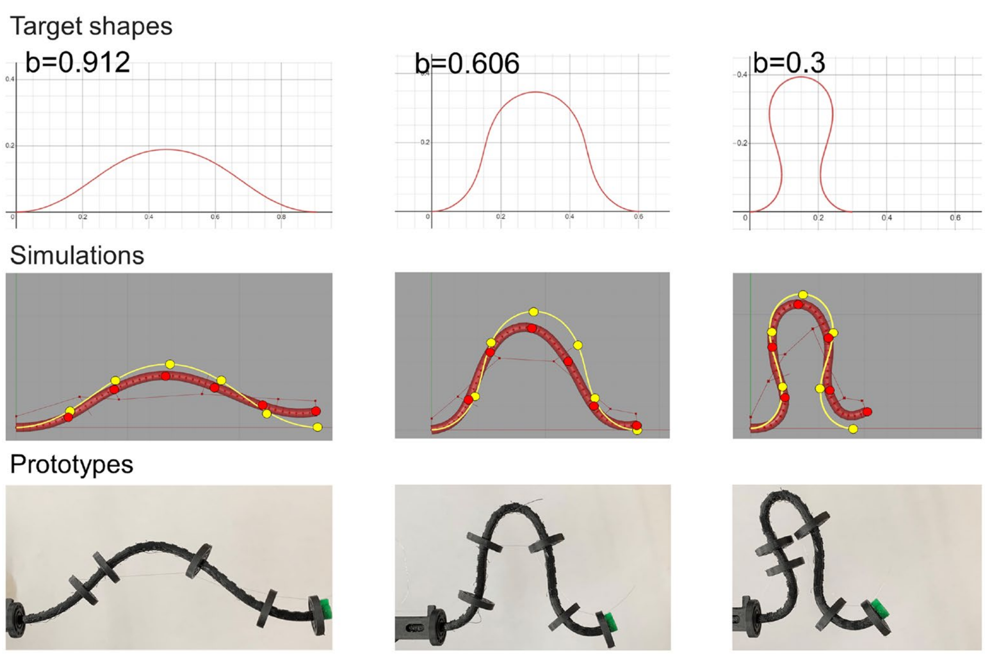


**Fig. 11** Target shapes and deformed shapes of simulations and prototypes. Deformed shapes are achieved by optimization of Penetration Model (ii). **a** $b = 0.912$. **b** $b = 0.606$. **c** $b = 0.3$

**Table 4** Optimization result of penetration model (ii)

| Unit [mm] | $w$ | $d_1$ | $d_2$ | $d_3$ | $d_4$ | $d_5$ |
|---|---|---|---|---|---|---|
| (a) $b = 0.912$ | 24 | 35 | 15 | 45 | 35 | 20 |
| (b) $b = 0.606$ | 55 | 25 | 25 | 45 | 35 | 20 |
| (c) $b = 0.3$ | 75 | 35 | 10 | 45 | 40 | 20 |

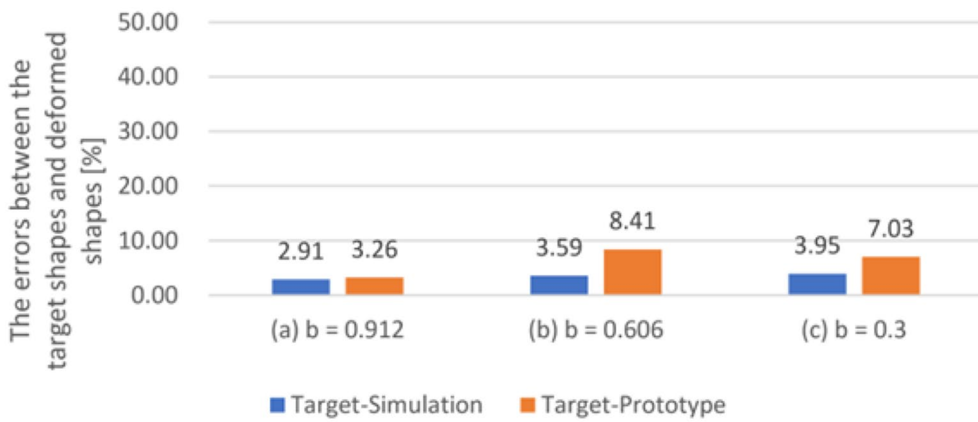


**Fig. 12** The error comparison between the target and deformed shapes (Penetration Model (ii))

The range of lengths of $d_n$ becomes narrower as the number of disc is increased, and the total length of the rod remains the same. In this case, the deformed shape of the continuum robot is close to the shape approximated by the constant curvature model. This limits the variation of the target shape that can be fitted. Meanwhile, decreasing the number of discs reduces the segments that can be partially fitted to the curvature of the target shape. Therefore, the optimal number of discs depends on the target shape and the total length of the rod.

An even greater variety of behaviors can be achieved by increasing the number of actuators and tendons. When the users set multiple target shapes, they need to perform the optimization process in this paper for each shape. Each deformed shapes can be made closer to the target shapes. We can combine those target shapes by adjusting the amount of tendon winding for each actuator.

## Conclusion and further work

In this paper, we proposed a method for a complexly deforming continuum robot that cannot be represented by the conventional constant curvature model using a single motor drive by adequately positioning the discs on the rod. We achieved this by using the proposed mathematical model and a genetic algorithm to search for the parameters (winding length of the tendon, $w$, segment lengths, $d_n$, and segment number to be drilled, $j$) to deform the rod close to the target curve. We simulated complex deformations by taking into account the tendon tension equilibrium. The average error for total rod length was less than 4% in the simulation and approximately 10% in the prototype.

The approximation errors were less than or equal to that of the constant curvature model obtained in previous studies (e.g., [23, 24]). The solution obtained by the optimization was adapted to prototypes. It was confirmed that deformations close to the target shape were obtained.

When the target shapes are known, the results obtained in this study provide optimal configurations of continuum mechanisms along the shape. For example, to explore complex environments, the continuum robot not only deforms passively in response to the environment but also actively along the path to enable the tip to access its destination readily. When grasping an object, the continuum mechanism actively deforms to the object shape, which is the target shape. For surface irregularities, the continuum mechanism deforms passively for fitting. The two types of deformation enable the grasping of an object.

Another application would be to design soft robots that mimic organisms that exhibit specific deformed shapes. For example, it is known that a clothoid curve can approximate the shape of a plant vine [25]. When making a robot hand that imitates this curve, it is possible to give it a configuration in which the deformed shape is close to this curve. It can also be used to build a robot that mimics the gait of a caterpillar [26]. By using the deformed shape of the actual caterpillar's body as the target shape, it is possible to reproduce the shape partially [22, 27]. In this paper, the rod was deformed by a DC motor. If a small actuator (such as an SMA actuator) can control the position of the disc dynamically, we can switch multiple target shapes. The overall size and weight of the robot can be reduced while maintaining the same degree of freedom and workspace.

**Acknowledgements**
We would like to thank Editage (www.editage.com) for English language editing.

**Author contributions**
D.Y. and T.U. conceived of the presented idea. D.Y. and T.U developed the theory and, D.Y. performed the computations. S.M. verified the analytical methods. T.U. supervised the findings of this work. All authors discussed the results and contributed to the final manuscript.

**Funding**
This work was supported by KAKENHI Grant-in-Aid for Scientific Research on Innovative Areas "Science of Soft Robot" project funded by JSPS under Grant Number 18H05467, and Grant-in-Aid for Scientific Research (B) under Grant Number 21H01289.

**Availability of data and materials**
Not applicable.

## Declarations

**Ethics approval and consent to participate**
Not applicable.

**Consent for publication**
Not applicable.

**Competing interests**
The authors declare that they have no competing interests.

Received: 28 December 2022 Accepted: 3 July 2023
Published online: 19 July 2023

**References**

1. Hirose S, Morishima A (1990) Design and control of a mobile robot with an articulated body. Int J Rob Res 9(2):99–114
2. Chirikjian GS, Burdick JW (1994) A hyper-redundant manipulator. IEEE Robo Automa Magaz 1(4):22–29
3. Simaan N, Xu K, Wei W, Kapoor A, Kazanzides P, Taylor R, Flint P (2009) Design and integration of a telerobotic system for minimally invasive surgery of the throat. Int J Robot Res 28(9):1134–1153
4. Crews JH, Buckner GD (2012) Design optimization of a shape memory alloy-actuated robotic catheter. J Intell Mat Syst Struct 23(5):545–562
5. Tsukagoshi H, Kitagawa A, Segawa M (2001) Active hose: An artificial elephant's nose with maneuverability for rescue operation. In: Proceedings 2001 ICRA. IEEE International Conference on Robotics and Automation (Cat. No. 01CH37164), vol. 3, pp. 2454–2459. IEEE
6. Jones BA, Walker ID (2006) Kinematics for multisection continuum robots. IEEE Trans Robot 22(1):43–55
7. Geng S, Wang Y, Wang C, Kang R (2018) A space tendon-driven continuum robot. In: International Conference on Swarm Intelligence, pp. 25–35. Springer
8. Davies JBC, Lane D, Robinson G, O'Brien D, Pickett M, Sfakiotakis M, Deacon B (1998) Subsea applications of continuum robots. In: Proceedings of 1998 International Symposium on Underwater Technology, pp. 363–369. IEEE
9. Davies JBC, Lane D, Robinson G, O'Brien D, Pickett M, Sfakiotakis M, Deacon B (1998) Subsea applications of continuum robots. In: Proceedings of 1998 International Symposium on Underwater Technology, pp. 363–369. IEEE
10. Clark AB, Mathivannan V, Rojas N (2020) A continuum manipulator for open-source surgical robotics research and shared development. IEEE Trans Med Robot Bionics 3(1):277–280
11. Trivedi D, Rahn CD, Kier WM, Walker ID (2008) Soft robotics: biological inspiration, state of the art, and future research. Appl Bionics Biomech 5(3):99–117
12. Burgner-Kahrs J, Rucker DC, Choset H (2015) Continuum robots for medical applications: a survey. IEEE Trans Robot 31(6):1261–1280
13. Grassmann RM, Rao P, Peyron Q, Burgner-Kahrs J (2022) Fas-a fully actuated segment for tendon-driven continuum robots. Front Robot AI. https://doi.org/10.3389/frobt.2022.873446/full
14. Ouyang B, Liu Y, Sun D (2016) Design and shape control of a three-section continuum robot. In: 2016 IEEE International Conference on Advanced Intelligent Mechatronics (AIM), pp. 1151–1156. IEEE
15. Nguyen T-D, Burgner-Kahrs J (2015) A tendon-driven continuum robot with extensible sections. In: 2015 IEEE/RSJ International Conference on Intelligent Robots and Systems (IROS), pp. 2130–2135 . IEEE
16. Yang Z, Yang L, Xu L, Chen X, Guo Y, Liu J, Sun Y (2021) A continuum robot with twin-pivot structure: The kinematics and shape estimation. In: International Conference on Intelligent Robotics and Applications, pp. 466–475. Springer
17. Webster RJ III, Jones BA (2010) Design and kinematic modeling of constant curvature continuum robots: A review. Int J Robot Res 29(13):1661–1683
18. Oliver-Butler K, Till J, Rucker C (2019) Continuum robot stiffness under external loads and prescribed tendon displacements. IEEE Trans Robot 35(2):403–419
19. Pogue C, Rao P, Peyron Q, Kim J, Burgner-Kahrs J, Diller E (2022) Multiple curvatures in a tendon-driven continuum robot using a novel magnetic locking mechanism. In: 2022 IEEE/RSJ International Conference on Intelligent Robots and Systems (IROS), pp. 472–479. IEEE
20. Image dimension measurement tool "Click Measure". https://onochi-lab.com/sdm_downloads/sdm_downloads-867/. Accessed 12 June 2023
21. Jian X, Zou T (2022) A review of locomotion, control, and implementation of robot fish. J Intell Robo Syst 106(2):1–27
22. Plaut RH (2015) Mathematical model of inchworm locomotion. Int J Non-Linear Mech 76:56–63
23. Kato T, Okumura I, Kose H, Takagi K, Hata N (2016) Tendon-driven continuum robot for neuroendoscopy: validation of extended kinematic mapping for hysteresis operation. Int J Comput Assis Radiol Surg 11(4):589–602
24. Kato T, Okumura I, Song S-E, Golby AJ, Hata N (2014) Tendon-driven continuum robot for endoscopic surgery: preclinical development and validation of a tension propagation model. IEEE/ASME Trans Mechatron 20(5):2252–2263
25. Fan J, Visentin F, Dottore ED, Mazzolai B (2020) An image-based method for the morphological analysis of tendrils with 2d piece-wise clothoid approximation model. In: Conference on Biomimetic and Biohybrid Systems, pp. 80–91. Springer
26. Koh J-S, Cho K-J (2010) Omegabot: Crawling robot inspired by ascotis selenaria. In: 2010 IEEE International Conference on Robotics and Automation, pp. 109–114. IEEE
27. Ghanbari A, Rostami A, Noorani SMRS, Fakhrabadi MMS (2008) Modeling and simulation of inchworm mode locomotion. In: International Conference on Intelligent Robotics and Applications, pp. 617–624 . Springer

## Publisher's Note

Springer Nature remains neutral with regard to jurisdictional claims in published maps and institutional affiliations.